# Theoretical Spectral Analysis of the IR-UWB Radar Chest Reflection with Arbitrary Periodic Breathing- and Heart-Induced Displacements

**Van Nguyen\* and Mary A. Weitnauer**

**Abstract**—The moving chest wall imparts a delay modulation onto the reflected IR-UWB radar signal, making the radar return a nonlinear function of chest wall displacement. Existing theoretical spectral models of the IR-UWB radar reflections from the human chest wall have restrictive assumptions that preclude realistic modeling of chest wall displacement and assume an aliased version of the radar signal. This paper presents novel theoretical analysis of the un-aliased spectrum, without the restrictive assumptions. Potential applications not specifically treated in this paper, but illustrative of the novelty and broader scope of the presented analysis, include heart-induced displacements that are realistically more bursty in nature and breathing-induced displacements consistent with, for example, non-unity inspiration-to-expiration ratios characteristic of asthma; neither of these could be analyzed using previous models. As well known, the un-aliased spectrum cannot generally be recovered from the aliased spectrum. In particular, the paper shows that the clusters of the non-aliased spectrum are not just scaled versions of each other; rather they have complex variations that if measurable, could enable estimation of parameters such as displacement amplitude; such variations are not apparent in the existing aliased spectrum model, which has just one cluster. This paper analyzes the degree to which the aliased model differs from the non-aliased model. The paper also addresses some practical aspects of the spectral model, such as the number of significant components in a spectral cluster and computational complexity of the theoretical model.

## 1. INTRODUCTION

Impulse radio Ultrawideband (IR-UWB) radar is a promising tool for non-contact physiological sensing, with applications including continuous health monitoring, breast tumor detection, search and rescue for trapped survivors under rubble, and surveillance [1–9]. Detecting respiration rate (RR) and heart rate (HR) by processing the chest-reflected IR-UWB radar signal attracts much research effort [10–16]. An alternative for RR and HR detection is continuous wave radar technology [17–19]. However, the IR-UWB radar has an advantage over the continuous wave radar in that the former is not only robust against interference from coexisting systems but also causes negligible interference to these systems, because of its extremely low power spectral density [20].

An IR-UWB system transmits a series of extremely low power and extremely short electromagnetic pulses, typically on the order of a nanosecond wide [21]. When these pulses fall on boundaries between materials with different dielectric properties, such as the skin-air interface, the pulses are reflected back to the IR-UWB receiver. Movements of the interface caused by breathing and heartbeats will induce changes in the round-trip propagation delays; hence the received signal is delay-modulated. This paper presents an analytical model of the chest-reflected signal arriving at the receive antenna that improves

upon existing research by realistically modeling chest movements, providing closed-form expression of the spectrum components, and removing the restrictive assumptions of previous models.

Analytical signal modeling is a foundation of many signal processing designs in many fields. For example, factorization of the power pattern in the spectral domain is used in the synthesis of shaped beams [22] in antenna theory. In audio engineering, the Fourier-Bessel decomposition of a soundfield into spherical harmonics forms the basis of sound spatialization techniques [23]. In estimation theory, an accurate theoretical model is essential in problem formulation, especially in model-based estimation methods such as maximum likelihood estimation and sequential Bayesian filtering [24, 25].

To our knowledge, only three different groups provide an analytical model of the IR-UWB received signal [14–16]. However, these models do not address realistic models of typical chest movements. These includes breathing patterns with non-unity inspiration-to-expiration ratio [26], not modelled well with just one or two sinusoids as assumed in [14–16], or bursty heartbeat displacement [27, 28], not consistent with just one sinusoid as in [16]. In addition, the existing models are derived for an *undersampled* version of the radar received signal. Undersampling causes the spectrum to be aliased, and generally the operation is not invertible [29]. In an effort to reverse-engineer the analog processing of a commercial IR-UWB vital signs monitor [30] from its digital samples, we needed a model that can apply to a type of direct down-conversion receiver that produces un-aliased samples [30]. Since the spectrum of the original continuous signal cannot generally be constructed from the aliased spectrum [29], we cannot simply apply the models of [14–16] to our problem. Therefore, there is a need for an unaliased IR-UWB spectral model that accommodates an arbitrary periodic chest displacement pattern, i.e., a pattern with an arbitrary number of sinusoidal components.

Additionally, the current models impose a restrictive assumption that the phases of all the sinusoids in the displacement model are equal and zero. That is, the phases of the sinusoidal breathing-induced displacement and the sinusoidal heart-induced displacement are assumed to be equal and zero [16]; the phase of the breathing-induced chest movement [14] or chest and abdomen displacements [15] are also assumed to be zero. In reality, there is no guarantee that, at data acquisition time, the breathing phase is zero and the relative phase of the heart and breathing is zero. A non-zero phase in the displacement model generally introduces an additional sinusoid, and existing analytical models cannot be applied and rederivation is needed. There appears to be no easy way and no guidance from these authors on how to convert the results if the displacement model changes, e.g., when a non-zero phase is present in the sine(s) in the model, or the sinusoids do not have equal phase. Thus, when a new pulse delay model is of interest, one generally has to re-derive the expressions in [14–16]. In contrast, our model eliminates this restrictive assumption by allowing an arbitrary periodic displacement model, and has final expressions that can be easily modified to accommodate changes.

In this paper, we present an analytical model that eliminates these limitations of the existing works. Our model, derived for the chest-reflected IR-UWB signal as it arrives at the receive antenna, allows an arbitrary periodic displacement model and provides the un-aliased spectrum. We show that the aliased and un-aliased spectra are substantially different. This paper significantly expands on the preliminary results reported in [31]. First, we perform an investigation into a special case of sinusoidal breathing and heart beating, which reveals the non-trivial dependence of the heights of the spectral peaks on the maximum chest displacement. Next, quantification of the difference between the aliased model of [14–16] and our un-aliased model is obtained. Practicality and usage of our model in terms of the number of significant terms and numerical precision are analyzed. Complete proof and numerical check of the model is given. Computation complexity comparison with direct application of the continuous-time Fourier transform (CTFT) is detailed. An example of model usage is also included.

Our analysis approach, which avoids the "fast time, slow time" formulation in [14–16], yields a model that is amenable to various applications. This model presents the Fourier coefficients in closed-form for a transmitted periodic pulse waveform and a single chest interface, assumed to be planar and displace according to the periodic lungs and heart motion. The resulting expressions constitute a tool that other researchers can use to analyze any periodic transmit waveform, e.g., periodic pseudo-random binary sequences [32], any periodic displacement pattern of the interface, and any planar multi-layered reflecting interface by applying well-known Fourier techniques. The model exposes the effects of aliasing and of different heart and lung displacement patterns. The paper gives an example of these applications. And since our model captures the signal as it arrives at the receiver antenna, it can be put with any

RF front end model to provide the radar received signal. In other words, our model is a critical core component that enables a full system model.

Our model should have several other uses. Spectral analysis is a common approach for vital signs estimation, but typical schemes focus only on the location of spectral peaks as a means of estimating rates [11–14, 16] and ignore peak heights. In contrast, the model reported herein will allow investigation into how breathing and heart *patterns* of movement impact the *shape* of the IR-UWB spectrum. For example, our findings show that the heights of the spectral peaks in the received spectrum depend on the maximum chest displacement; we note this is not a trivial dependence in delay modulation, which is a non-linear modulation. In addition, our model is not restricted to only the moving planar chest wall, but is also applied to any electro-magnetic wave reflected by a planar interface that displaces periodically. For example, a potential application could be detection of certain motors or machines by their vibration pattern.

An example plot of the Fourier spectrum produced by our model is shown in Fig. 1. The RR fundamental component $(f_b)$ and its next harmonics $(2f_b, 3f_b)$, the HR fundamental $(f_h)$, and some intermodulation products (*intermods*), e.g., $f_b + f_h$, are clearly observed. Unfortunately, we do not have a fully characterized IR-UWB radar system that would enable us to compare our theoretical spectrum with a measured spectrum. However, the spectrum produced by our model in Fig. 1 does compare favorably to the measured spectrum shown in Fig. 13(b) in [16]. For Fig. 1, we tried to match the parameters of the measured spectrum in [16]. In particular, we set the observation window to be rectangular with a length of 32 s, the HR is the ground-truth HR reported in [16], and the RR is selected to be the frequency of the highest peak in the measured spectrum since its ground-truth is not provided. We also selected the displacement amplitudes to give similar relative heights of the peaks at the breathing and heart fundamentals. The UWB pulse used was a Gaussian monocycle [33] of order 7 with the bandwidth scaling factor of 0.3 ns, whose waveform is similar to the pulse waveform in [16]. The pulse shape and its Fourier transform are plotted in Fig. 2. Other parameters for this example are discussed in Section 3.2. Since our model is a decomposition of the signal part of the radar received spectrum, receiver noise will be ignored in our analysis, but noise can always be added to the model
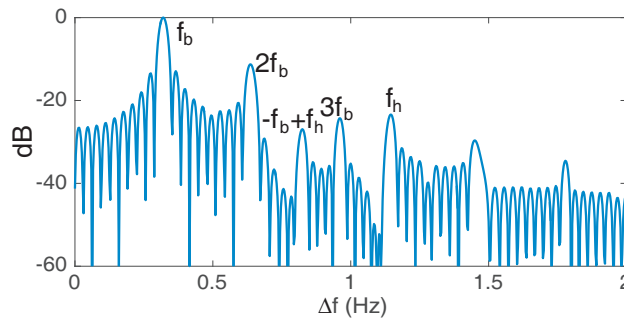


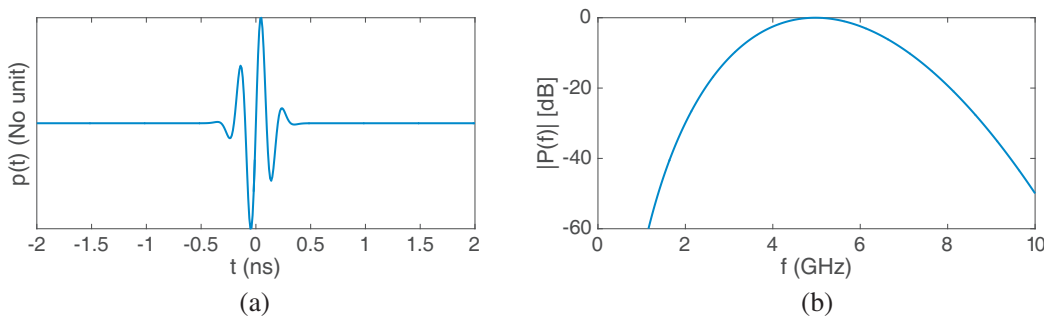**Figure 1.** An example of a radar received spectrum obtained with our model.



**Figure 2.** Gaussian monocycle of order 7 and bandwidth scaling factor of 0.3 ns. (a) Time-domain waveform $p(t)$. (b) Spectrum $P(f)$.

presented herein.

The paper is organized as follows. Section 2 presents our general result. The special case of the sum-of-two-sinusoids chest displacement model in [16] is addressed in Section 3. Practicality and computational complexity comparison with direct application of the CTFT are discussed in Sections 4 and 5. Conclusion follows.

## 2. DERIVATION OF THE GENERAL CASE

This section starts with a base model, derived for the case of transmitted perfect impulses and a rectangular observation window of infinite length. We then show how the base model is readily modified for any UWB pulse or burst shape, any observation window of finite length, and when the received signal comprises back-scattered components from multiple layers of the thorax. Finally, an example of model usage is given.

The received signal is assumed to contain only the reflection from the air-skin interface, modeled as an infinite plane [†]. The periodic chest displacement is modeled as a summation of a periodic breathing-induced displacement and a periodic heartbeat-induced displacement, each of which is represented by a Fourier series expansion. Therefore, the round-trip propagation delay caused by chest displacement of an UWB pulse or burst can be modeled as

$$\tau_d(t) = A_0 + \sum_{p=1}^{N_b} \left[ B_p^b \sin 2\pi(pf_b)t + A_p^b \cos 2\pi(pf_b)t \right] + \sum_{q=1}^{N_h} \left[ B_q^h \sin 2\pi(qf_h)t + A_q^h \cos 2\pi(qf_h)t \right], \quad (1)$$

where $f_b$ is the respiration rate [Hz]; $f_h$ is the heart rate [Hz]; $N_b$ and $N_h$ are the numbers of non-DC Fourier series coefficients of the breathing-induced delay and the heartbeat-induced delay, respectively. $A_0$ combines the DC components of the breathing-induced and heartbeat-induced delays and the delay due to the nominal distance between the radar and the subject's chest. Note that there is no assumption on the phase of the breathing-induced delay and the phase of the heartbeat-induced delay; they are incorporated in the Fourier series coefficients $\{B_p^b, A_p^b, B_q^h, A_q^h : p = 1, \ldots, N_b; q = 1, \ldots, N_h\}$.

The IR-UWB radar system transmits pulses or short bursts with the repetition period of $T_r$. Assuming the chest location is constant for the duration of the pulse or burst, the round-trip delay of the $n$-th pulse or burst can be represented as the $n$-th sample of $\tau_d(t)$ with the time sampling interval equal to $T_r$: $\tau_{d,n} = \tau_d(nT_r)$, where $\tau_d(t)$ is given in (1).

### 2.1. Base Model — Perfect Impulses Are Transmitted

Assuming that motion filtering rejects static clutter [14, 16], a planar chest model, and that the received signal contains only reflection from the skin-air interface, the sole channel effect is one time-varying delay, so the impulse response is simply a delayed Dirac delta function such that the delay is a periodic function of time. Constant amplitude reductions, e.g., due to path loss, are ignored, since they would have the effect of simply scaling the received signal spectrum.

The channel response to a periodic train of impulses with period $T_r$, is

$$h(t) = \sum_{n=-\infty}^{\infty} \delta(t - nT_r - \tau_{d,n})$$

and is illustrated in Fig. 3 for the chest displacement modeled as a sine waveform. The CTFT of $h(t)$ is $H(f) = \sum_{n=-\infty}^{\infty} e^{-j2\pi f(nT_r + \tau_{d,n})}$ and is derived in the appendix using Fourier theory and Jacobi-Anger expansions to be

$$H(f) = \sum_i \sum_{k_1} \cdots \sum_{k_{N_b}} \sum_{k_1'} \cdots \sum_{k_{N_b}'} \sum_{l_1} \cdots \sum_{l_{N_h}} \sum_{l_1'} \cdots \sum_{l_{N_h}'} c(f_{\mathbf{z}}) \delta\left(f - f_{\mathbf{z}}\right), \quad (2)$$

---

[†] As in [14–16], we assume that the environment is static so the only motion that modulates the radar signal is from the movement induced by breathing and heart beating. Each recorded waveform is a superposition of a pulse reflected from the moving chest and pulses reflected from the static clutter. A "motion filter" [14–16] suppresses the static clutter-reflected pulses but retains the moving-chest-reflected pulses.
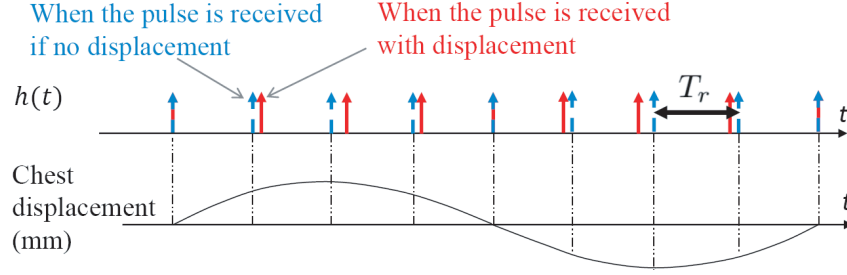
**Figure 3.** The channel response of the physiological sensing IR-UWB radar system to a series of impulses for sine chest displacement. Blue: zero displacement. Red: sinusoidal displacement.

where $\mathbf{z} = [k_1, \ldots, k_{N_b}, k'_1, \ldots, k'_{N_b}, l_1, \ldots, l_{N_h}, l'_1, \ldots, l'_{N_h}, i]$, $f_{\mathbf{z}} = [\sum_{p=1}^{N_b} p(k_p + k'_p)]f_b + [\sum_{q=1}^{N_h} q(l_q + l'_q)]f_h + if_r$,

and

$$
\begin{aligned}
c(f) \; = \; & f_r \times (-1)^{\sum_{p=1}^{N_b} k_p + \sum_{q=1}^{N_h} l_q} \times (-j)^{\sum_{p'=1}^{N_b} k'_{p'} + \sum_{q'=1}^{N_h} l'_{q'}} \\
& \times \prod_{p=1}^{N_b} J_{k_p}(2\pi B_p^b f) \prod_{p'=1}^{N_b} J_{k'_{p'}}(2\pi A_{p'}^b f) \prod_{q=1}^{N_h} J_{l_q}(2\pi B_q^h f) \prod_{q'=1}^{N_h} J_{l'_{q'}}(2\pi A_{q'}^h f) e^{-j2\pi A_0 f},
\end{aligned}
$$

where $f_r = 1/T_r$ is the pulse repetition frequency.

The above model maps a decomposition of the displacement model into a decomposition of the received spectrum. Several observations can be made about the spectral decomposition.

(i)   The spectral component locations, represented by $f_{\mathbf{z}}$, are multiples of RR, multiples of HR, multiples of the pulse repetition frequency, and their intermods $kf_b + lf_h + if_r$, where $k, l, i$ are integers. In existing models, the frequencies do not contain multiples of the pulse repetition frequency.

(ii)  The coefficients are expressed in closed-form. Existing models express the spectral coefficients as an integral over the entire bandwidth of the product of the pulse spectrum and one [14], two [16], or three [15] Bessel functions, or even more for a higher number of sinusoids in the pulse delay model, which does not have closed form.

(iii) The coefficients are a function of $f_b, f_h, f_r$, and the Fourier series coefficients in the delay model (1). This allows investigation into how breathing and heart patterns of movement impact the shape of the IR-UWB received spectrum. In existing models, the coefficients do not depend on $f_b, f_h, f_r$.

This spectrum model, derived for a single-tap channel model with unity coefficient, can be easily extended to the case of a multi-tap channel model with arbitrary time-varying coefficients by using the principle of superposition. Such an extended model could be applied to a multi-layer model of the human thorax. Further details on the extension will be presented in Section 2.4.

## 2.2. UWB Pulses or Burst Waveforms Are Transmitted

Let $p(t)$ be the transmit UWB burst waveform and $P(f)$ be its CTFT[‡]. The radar received signal is $y(t) = p(t) * h(t)$ and its CTFT is $Y(f) = P(f)H(f)$. It follows that $Y(f)$ is equal to the right hand side of Eq. (2) after replacing $c(f_{\mathbf{z}})$ with $g(f_{\mathbf{z}}) = c(f_{\mathbf{z}})P(f_{\mathbf{z}})$. The observations in Section 2.1 also apply here.

## 2.3. Finite Observation Window

The model in Eq. (2) assumes an infinite record of the received signal. Let $w(t)$ be the observation window of finite duration and $W(f)$ be its Fourier transform. In the case of a finite observation

---

[‡] For instance, $p(t)$ can be a pseudo-random binary-modulated waveform or just a simple pulse, as in [14–16]

window, the channel response to a periodic train of impulses is $h_w(t) = h(t)w(t)$. Its CTFT is $H_w(f) = H(f) * W(f)$ and is equal to the right hand side of Eq. (2) after replacing "$\delta$" with "$W$".

Similarly, the channel response to a periodic train of UWB bursts, observed over a finite time window, is expressed as $y_w(t) = y(t)w(t)$, and its CTFT is $Y_w(f) = Y(f) * W(f)$, where $Y_w(f)$ is equal to the right hand side of Eq. (2) after replacing $c(f_{\mathbf{z}})$ with $g(f_{\mathbf{z}}) = c(f_{\mathbf{z}})P(f_{\mathbf{z}})$ and "$\delta$" with "$W$".

**Table 1.** Mapping between a term in Eq. (1) and a summation in Eq. (2).

| (1) | $\sin 2\pi(pf_b)t$ | $\cos 2\pi(pf_b)t$ | $\sin 2\pi(qf_h)t$ | $\cos 2\pi(qf_h)t$ |
|---|---|---|---|---|
| (2) | $\sum\limits_{k_p}$ | $\sum\limits_{k'_p}$ | $\sum\limits_{l_q}$ | $\sum\limits_{l'_q}$ |

### 2.4. Extension to a Multi-Layer Chest Model

Let $S$ be the number of body tissues layers that move periodically due to breathing and/or heart beating. For the infinite observation window case, the channel response to a periodic train of impulses is $h(t) = \sum\limits_{n=-\infty}^{\infty} \sum\limits_{s=1}^{S} \mu^{(s)}(t)\, \delta(t - nT_r - \tau_{d,n}^{(s)}) = \sum\limits_{s=1}^{S} \mu^{(s)}(t) \sum\limits_{n=-\infty}^{\infty} \delta(t - nT_r - \tau_{d,n}^{(s)})$, where $\mu^{(s)}(t)$ and $\tau_{d,n}^{(s)}$ are the amplitude and delay of the tap modeling the $s^{\text{th}}$ layer.

By Fourier Transform and the principle of superposition, the CTFT of $h(t)$ is $H(f) = \sum\limits_{s=1}^{S} \mathscr{F}\{\mu^{(s)}(t)\} * H^{(s)}(f)$ where $H^{(s)}(f)$ is Eq. (2).

The extension for the variations of $H(f)$, $H_w(f)$, $Y(f)$ and $Y_w(f)$, can be done in a similar straightforward manner.

### 2.5. Example of Model Usage

Our model describes how each component in the Fourier decomposition of the displacement model contributes to the received the spectrum. Each sinusoidal term in the delay model in Eq. (1) corresponds to a summation in the radar received spectrum model in Eq. (2) (and its variations $H_w(f), Y(f)$ and $Y_w(f)$), as shown in Table 1. In other words, if the displacement model lacks a particular sinusoidal component, the corresponding summation will not be needed in the spectrum. For example, assume that $\tau_d(t) = B^b \sin 2\pi f_b t + A_1^h \cos 2\pi f_h t + A_2^h \cos 4\pi f_h t$. In this example, the delay due to breathing-induced displacement is modeled as a sine, and the delay due to heartbeat-induced displacement is modeled as a sum of two cosines whose frequencies are the HR and its next harmonic. The spectrum model in Eq. (2) becomes $H(f) = \sum_i \sum_{k_1} \sum_{l'_1} \sum_{l'_2} c(f_{\mathbf{z}})\, \delta(f - f_{\mathbf{z}})$, where $f_{\mathbf{z}} = k_1 f_b + (l'_1 + 2l'_2)f_h + if_r$ and $c(f) = f_r(-1)^{k_1}(-j)^{l'_1+l'_2} J_{k_1}(2\pi B_1^b f) J_{l'_1}(2\pi A_1^h f) J_{l'_2}(2\pi A_2^h f)$.

This example and discussion illustrate how this model, unlike the models of [14–16], do not have to be rederived as the chest displacement model changes.

## 3. SPECIAL CASE OF SINUSOIDAL BREATHING AND HEART BEATING

In this section, application of the general model in Section 2 to the special case of sinusoidal breathing and sinusoidal heart beating is presented, and features that differentiate our model from existing aliased models are clarified.

Specifically, we will use the displacement model assumed in [16], which is a sum of two sines with zero phase representing the breathing-induced and heartbeat-induced displacements, respectively. Mathematically, the delay due to this chest displacement model is written as

$$\tau_d(t) = A_0 + A_b \sin 2\pi f_b t + A_h \sin 2\pi f_h t, \tag{3}$$

where $A_0$ is the delay due to the nominal distance between the radar and the chest [16].

### 3.1. Infinite Observation Window

From Eq. (2), the CTFT of the channel response to the periodic train of impulses with period $T_r$ can be expressed as

$$H(f) = \sum_{i=-\infty}^{\infty} \sum_{k=-\infty}^{\infty} \sum_{l=-\infty}^{\infty} c(f_{\mathbf{z}}) \cdot \delta(f - f_{\mathbf{z}}), \qquad (4)$$

where $f_{\mathbf{z}} = kf_b + lf_h + if_r$ and $c(f) = f_r(-1)^{k+l}J_k(2\pi A_b f) \, J_l(2\pi A_h f)e^{-j2\pi A_0 f}$.

The radar received signal spectrum with a received burst shape $p(t)$, $Y(f)$, is equal to the right hand side of Eq. (4) after replacing $c(f_{\mathbf{z}})$ with $g(f_{\mathbf{z}}) = c(f_{\mathbf{z}})P(f_{\mathbf{z}})$.

As an example, suppose $f_r$, $f_b$, $f_h$, the breathing-induced chest displacement amplitude $m_b$, and the heartbeat-induced chest displacement amplitude $m_h$ take the values in Table 2. $A_b = 2m_b/\nu$, $A_h = 2m_h/\nu$, where $\nu = 3 \times 10^8$ m/s, $A_0 = 2d/\nu$, where the nominal distance between the radar and subject is $d = 30$ cm. The expression in Eq. (4) is evaluated with this parameter set over the frequency range of several multiples of $f_r$ in the GHz range. The magnitude of the resulting spectrum, $|H(f)|$, is plotted in Fig. 4.

A clustered structure with great sparsity is observed; the spectrum contains clusters centered at multiples of $f_r$, each of which contains spectral components that are away from the cluster center by $kf_b + lf_h$, where $k, l \in Z$. The magnitudes of the spectrum components in the cluster centered at $i_0 f_r = 5$ GHz, normalized to the magnitude of the cluster center component, are plotted in Fig. 5(a). The normalized components that are less than $-50$ dB are plotted in black. The rapid decay of the spectrum components as their order ($|k|$ and $|l|$) increases is observed. If $-50$ dB relative power level is considered as the lowest significant power, there are only 17 significant spectral components in this example, spanning just a few Hz, whereas the separation between the clusters is 250 kHz ($f_r$).
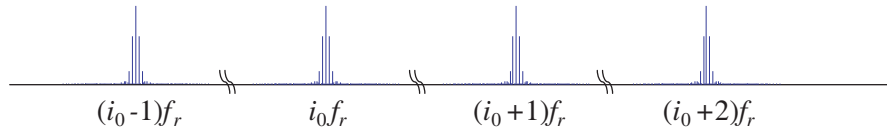


$(i_0 \text{-}1)f_r$ $\qquad\qquad$ $i_0 f_r$ $\qquad\qquad$ $(i_0 \text{+}1)f_r$ $\qquad\qquad$ $(i_0 \text{+}2)f_r$

**Figure 4.** An example of $|H(f)|$. In this example, $i_0 = 20,000$ and $f_r = 250$ kHz, thus the clusters are in the vicinity of 5 GHz. The space between the cluster has been shrunk to aid visibility of the spectrum components within each cluster.

**Table 2.** Example simulation parameter values.

| | | |
|---|---|---|
| Pulse repetition frequency | $f_r$ | 250 kHz |
| Window length | $T_w$ | 32 s |
| Maximum breathing displacement | $m_b$ | 5 mm |
| Respiration rate | $f_b$ | 0.3199 Hz |
| Maximum heart displacement | $m_h$ | 0.3571 mm ($m_b/14$) |
| Heart rate | $f_h$ | 1.14 Hz |

Although not obvious in Fig. 4, there is change in the magnitudes of the spectrum components from one cluster to the next. Fig. 5(b) plots the magnitudes of the cluster center, $f_b$, and $f_h$ components (which are $|c(f_{00i})|$, $|c(f_{10i})|$, and $|c(f_{01i})|$, respectively) across the clusters in the frequency range of 3–7 GHz. In addition to the parameter set above, the plots include $m_b$ set to two other values of 3.62 mm and 7.96 mm, $m_h = m_b/14$, while the other parameters stay the same. Fig. 5(b) shows that the clusters are not simply scaled versions of each other. In particular, for example, for $m_b = 7.96$ mm, which corresponds to the last three entries in the legend (i.e., the thickest, green curves), the cluster center component ($|c(f_{00i})|$, solid line) drops monotonically almost 30 dB over the band, while the $|c(f_{10i})|$ component (dotted) first rises a few dB and then drops slightly. The changing pattern of the 3-tuple
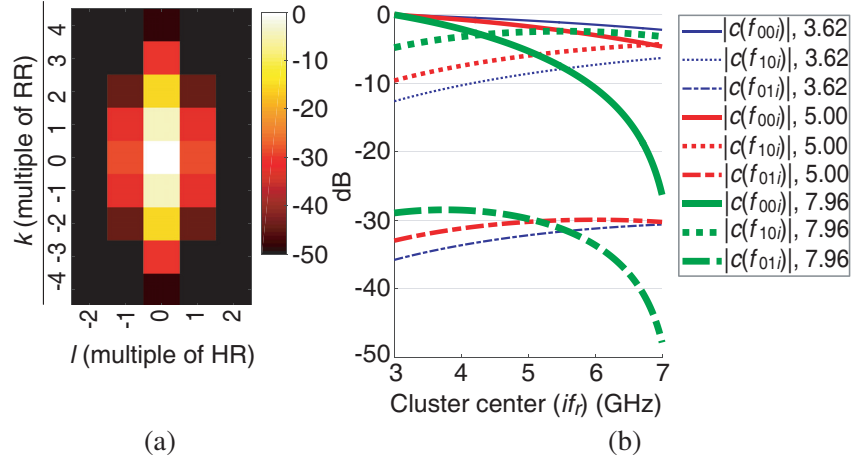
(a)                                    (b)

**Figure 5.** (a) The spectrum coefficients $c(kf_b + lf_h + i_0f_r)$, normalized to the cluster center and converted to dB, in the cluster centered at $i_0f_r$ in Fig. 4. These coefficients correspond to the frequencies $kf_b + lf_h + i_0f_r$. The normalized components that are less than $-50$ dB are plotted in black. (b) Magnitude variation of the cluster center, $f_b$, and $f_h$ components (which are $|c(f_{00i})|$, $|c(f_{10i})|$, and $|c(f_{01i})|$, respectively) for different values of the maximum breathing-induced displacement $m_b$ (the maximum heartbeat-induced displacement $m_h = m_b/14$). The values of $m_b$ in mm are shown at the end of the legend items.

group differs for different values of $m_b$; this suggests that $m_b$ might be estimated from measurements of widely spaced clusters.

## 3.2. Finite Observation Window

Following Section 2.3, we have

$$H_w(f) = \sum_{i=-\infty}^{\infty} \sum_{k=-\infty}^{\infty} \sum_{l=-\infty}^{\infty} c(f_{\mathbf{z}}) \cdot W(f - f_{\mathbf{z}}). \tag{5}$$

for transmitted impulses, and

$$Y_w(f) = \sum_{i=-\infty}^{\infty} \sum_{k=-\infty}^{\infty} \sum_{l=-\infty}^{\infty} P(f_{\mathbf{z}})c(f_{\mathbf{z}}) \cdot W(f - f_{\mathbf{z}}). \tag{6}$$

for transmitted UWB bursts with spectrum $P(f)$.

We calculate a very close approximation of $|Y_w(f)|$ for a rectangular window with $T_w = 32$ s and the same parameters as in the example in Section 3.1. This approximation is created from the 1600 most significant non-DC terms of Eq. (6), for the cluster centered at $i_0f_r$, that is $i = i_0$ and $1 \leq |k|, |l| \leq 20$; these include the 17 most significant terms excluding the center component (DC after down conversion) in Fig. 5(a). The calculated spectrum is shown in Fig. 1, where $\Delta f$ denotes the frequency relative to $i_0f_r$, the cluster center location. The RR fundamental component and its harmonics, the HR fundamental, and some intermods are clearly observed. More details on truncation are given in Section 4.

## 3.3. Features that Differentiate Our Work from that of [14–16]

The authors of [14–16] describe their waveforms in terms of "slow time" and "fast time". The slow time axis indicates each pulse repetition, while the fast time index resolves waveform features within a pulse repetition period, as shown in Fig. 6(a).

As in [14–16], we assume that the environment is static, so the only motion that modulates the UWB signal is from breathing and heart beating, and that a multipath profile, which is a waveform containing
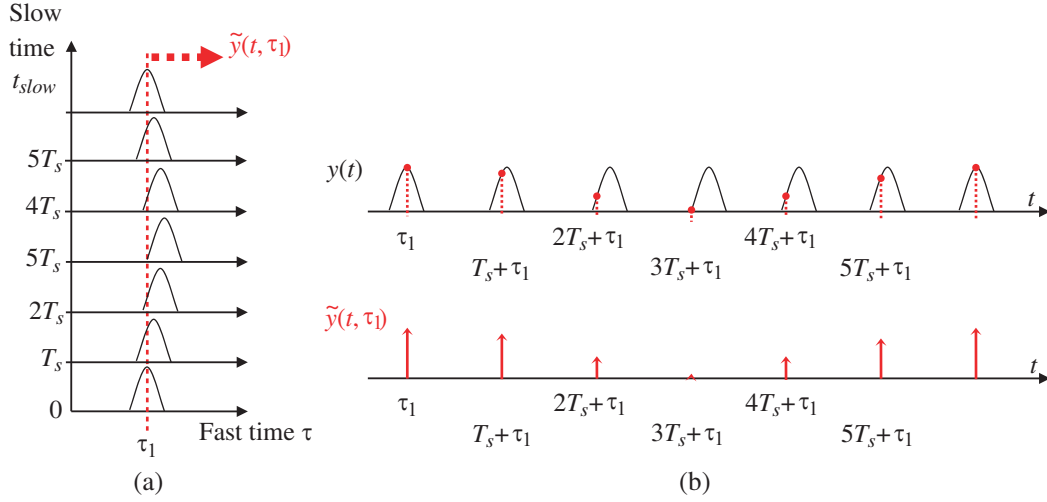
**Figure 6.** (a) Illustration of the signal analyzed in [14–16] in the (slow time, fast time) coordinate system: $\tilde{y}(t, \tau)$ for a given $\tau$ is the signal whose CTFT is computed in [14–16]. (b) Illustration of how it is related to the whole radar received signal on the 1D time axis.

the reflected pulses from static clutter and the moving chest, is recorded every $T_s$. We note that $T_s$ must not be confused with the sampling period associated with the sampling within each multipath profile, which is a fraction of the pulse width and can be in the order of picoseconds. Although not mentioned in these papers, $T_s$ must be an integer multiple of the repetition period, $T_r$. A "motion filter" [14, 16] passes the moving-chest-reflected pulses and suppresses the static clutter-reflected pulses [14–16]. The recorded waveforms after clutter removal are illustrated in the (slow time, fast time) coordinate system as in Fig. 6(a). The samples at a given value of $\tau_1$ in the waveforms form the signal whose spectrum is analyzed in [14–16]. This can be seen, for example, in Eq. (7) of [16]. By unifying the slow time and fast time into the actual one-dimensional time, as in the two plots of Fig. 6(b), it can be seen that the signal analyzed in [14–16] is obtained by sampling the received signal every $T_s$ with some sampling offset $\tau_1$ on the order of the pulse width. In other words, the sampling instants are $\tau_1, T_s + \tau_1, 2T_s + \tau_1, \ldots$ ($\tau_1$ should be thought as "fixed" in this context). This is an act of undersampling since the sampling rate is at most equal to the repetition frequency $f_r$, which is typically on the order of kHz or MHz and is smaller than the Nyquist rate which is on the order of GHz, thus causing aliasing, explained further as follows.

To compare with the aliased model in [14–16], infinite observation window case is used, since it is assumed in these papers. The spectrum of a sampled signal is well known to be

$$Y_a(f) = \frac{1}{T_s} \sum_{m=-\infty}^{\infty} Y\left(f - \frac{m}{T_s}\right), \tag{7}$$

which is periodic with period $\frac{1}{T_s}$. When $\frac{1}{T_s}$ is less than the Nyquist rate of $Y(f)$, the copies $Y(f - \frac{m}{T_s})$ for different $m$ overlap each other (this is aliasing), causing $Y_a(f) \neq Y(f)$ for at least some $f$ in every $\frac{1}{T_s}$ period [29]. Generally, we cannot use the spectrum expression in [14, 16], or [15] to construct the non-aliased spectrum of the whole radar received signal.

We can make the aliased spectrum using Eq. (7) and investigate numerically the differences between the aliased and un-aliased spectra. In order to avoid truncating the sum in a numerical evaluation, we assume $p(t)$ is a complex-exponentially-weighted sinc pulse such that its spectrum is a rectangle that spans $3\,\text{GHz} - f_r/2$ to $7\,\text{GHz} + f_r/2$. Considering Fig. 4[§], the aliasing would not distort the spectrum of a single cluster if the clusters were identical. However, since the clusters are not identical, as explained in Section 3.1, there is some distortion in the aliased spectra of [14–16]. For simplicity, suppose $T_s = T_r$.

---

[§] $Y(f) = P(f)H(f)$ has similar magnitude plot as in Fig. 4

Then $Y_a(f) = \frac{1}{T_r} \sum_{m=m_{\min}}^{m_{\max}} Y(f - \frac{m}{T_r})$, where $m_{\min} = i_0 - \lceil 7 \times 10^9 / f_r \rceil$ and $m_{\max} = i_0 - \lfloor 3 \times 10^9 / f_r \rfloor$. The range $[m_{\min}, m_{\max}]$ ensures that all the clusters from $3\,\mathrm{GHz}$ to $7\,\mathrm{GHz}$ are included in the summation when it is evaluated in the neighborhood of $i_0 f_r$, i.e., all these unaliased clusters contribute to the aliased cluster centered at $i_0 f_r$. Next, we compute

$$\mathrm{diffdB}(\Delta f) = 20 \log_{10} \frac{|Y(i_0 f_r + \Delta f)|}{|Y_a(i_0 f_r + \Delta f)|}$$

for selected values of $\Delta f$, and for 100 trials of breathing- and heartbeat-induced maximum displacements, including the $m_b$ and $m_h$ of the particular case of Fig. 4 and 99 random trials such that $m_b$ and $m_h$ are uniformly distributed, with $m_b \sim \mathcal{U}(2,8)\,[\mathrm{mm}]$ and $m_h \sim \mathcal{U}(2/128, 8/14)\,[\mathrm{mm}]$. $|Y(f)|$ and $Y_a(f)$ are normalized so their ratio is 1 at $f = i_0 f_r$, or $\mathrm{diffdB}(0) = 0\,\mathrm{dB}$, which corresponds to the second cluster from the left in Fig. 4. If the aliased spectrum is identical to the unaliased spectrum, $\mathrm{diffdB}(\Delta f) = 0$ for all values of $\Delta f$.

Figure 7 displays diffdB for various values of $\Delta f$, comprising harmonics and intermods. For a particular harmonic or intermod, the graph shows diffdB values for two examples of the random $m_b$ and $m_h$, indicated by an open circle and an open triangle. Also included is the particular case of Fig. 4, indicated by a green "x". For example, at $\Delta f = f_b = 0.3199\,\mathrm{Hz}$, the two random trials yield spectrum magnitude differences of about $5\,\mathrm{dB}$ and $14.4\,\mathrm{dB}$, and the Fig. 4 case gives a difference of about $-4.5\,\mathrm{dB}$. All the other random trial outcomes are plotted as blue dots, which for $\Delta f = f_b = 0.3199\,\mathrm{Hz}$, extend from about $-19\,\mathrm{dB}$ to $20\,\mathrm{dB}$. Finally, for each harmonic or intermod, the mean of the 100 diffdB values is plotted as a solid red square, and the first standard deviations away from the mean are indicated by red bars. We observe that for a given trial, e.g., indicated by triangles for instance, the diffdB values vary across harmonics and intermods. We also observe diffdB values as large in magnitude as $47\,\mathrm{dB}$, indicating significant differences between the aliased spectrum of [14–16] and the un-aliased spectrum presented in this paper. We have recomputed Fig. 7 for different kinds of representative UWB pulses (Gaussian monocycles of various orders and widths) [34] and similar differences are observed.

These results in Fig. 7 show that neither [14–16] nor any works by others, to our knowledge, provide the closed-form formulas for the unaliased spectrum, even for displacement defined by only a few sinusoids. Furthermore, because [14–16] only give one aliased cluster, variations across clusters caused by breathing patterns of clinical relevance cannot be known from existing works. While our
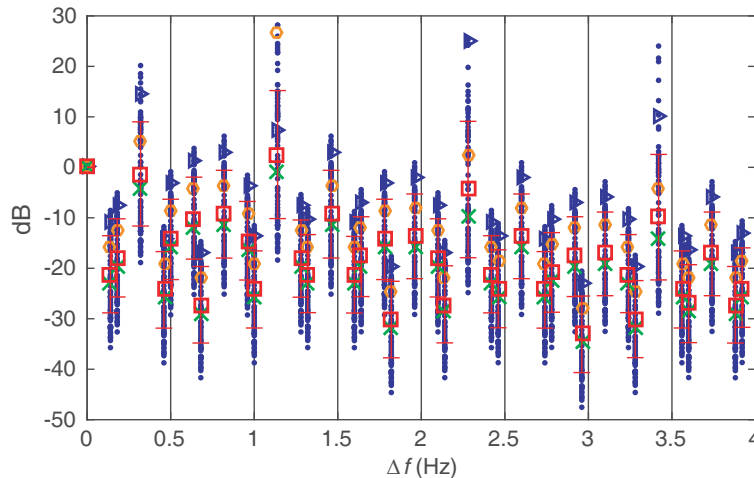


**Figure 7.** The relative power difference between the normalized un-aliased cluster centered at $i_0 f_r$ and the normalized aliased cluster over a frequency range for the example in Section 3.1 (shown by the green "x") and 99 random trials of $m_b$ and $m_h$. The relative power difference corresponding to two of these trials are shown with the triangle symbols and circle symbols respectively, and the other trials are represented by the small dots. The mean and standard deviation of the differences are also shown at each frequency location by a filled square and horizontal red bars.

model facilitates a study of such variations, we defer those results to a future report, because of space limitations in this paper. Finally, we note that for a given pulse shape, the amplitudes $g(f_{\mathbf{z}})$ in our model are functions of $f_b, f_h, f_r, A_b, A_h$ whereas the amplitudes in the model of [16] — Eq. (15) depend on only $A_b$ and $A_h$.

## 4. PRACTICALITY OF OUR ANALYTICAL MODEL

In this section, we discuss the practicality of our spectrum model and perform a numerical check on the accuracy of the mathematical derivation. Again, we start with the case of transmitted impulses. Extending the comparison to the case when UWB bursts are transmitted is straightforward and will be discussed at the end of this section.

Without loss of generality, assume the observation window is rectangular over $[-T_w/2, T_w/2]$. In this case, $h_w(t) = \sum_{n=-N}^{N} \delta(t - nT_r - \tau_{d,n})$, where $N = \lceil f_r T_w/2 \rceil$, and $\tau_{d,n} = \tau_d(nT_r)$, where we use the delay model $\tau_d(t)$ in (3). Therefore,

$$H_w(f) = \sum_{n=-N}^{N} e^{-j2\pi f(nT_r + \tau_{d,n})}. \tag{8}$$

The spectrum computed using Eq. (8) serves as ground truth, as it is based purely on the definition of the CTFT of a time-domain signal. Ideally, the spectrum computed using our synthesis formula (5) should be the same as the spectrum computed by Eq. (8). However, this is not feasible for two reasons. First, Eq. (5) requires evaluating the summations over unbounded integer indices $(k, l, i)$. Another reason is the presence of numerical computation error of the computing software used. Calculations of both the truth and the synthesized spectra include floating-point errors and numeric precision limitations. In this paper, all computation is implemented with double-precision floating-point arithmetic in MATLAB. The error also depends on the accuracy of the algorithm used by the computing software to compute the Bessel functions in Eq. (4) [35, 36]. Fortunately, as we will show shortly, a synthesized spectrum that accurately matches the ground truth can be achieved with very small ranges of the integer indices, i.e., with a very small number of spectral components or terms.

As seen in Fig. 4, the clusters are separated by $f_r$, which is on the order of kHz or MHz, and as Fig. 5(a) exemplifies, the spectrum components in each cluster decay precipitously just a dozen Hz away from the cluster center. Such sparsity indicates that, in the case of a practical finite window length, one cluster has negligible overlap or interference from other clusters. Therefore, although Eq. (5) indicates (through the outermost summation) that the spectrum is a superposition of the clusters, the spectrum, when evaluated in the neighborhood of a cluster, can be computed using the contribution of that cluster only. Furthermore, the decay of the high order harmonics and intermods as shown in Fig. 5(a) encourages the use of finite limits of $k$ and $l$ in the two innermost summations of Eq. (5). The decay is rapid, thus (the absolute value of) those limits should be small. In summary, the ground-truth spectrum can be well approximated by a truncated version of Eq. (5):

$$\widehat{H_w}(f) = \sum_{k=-K}^{K} \sum_{l=-L}^{L} c(f^*) \cdot W(f - f^*), \tag{9}$$

where $f^* = kf_b + lf_h + i_0 f_r$ and $K, L \ll \infty$, $f$ is in the vicinity of $i_0 f_r$.

As an example, suppose $T_w$, $f_r$, $f_b$, $f_h$, $m_b$, $m_h$ take the values in Table 2. Assume $A_0 = 0$ s. Although zero is not a practical value for $A_0$, it simplifies computation while not invalidating the comparison, because $A_0 > 0$ represents the same term $e^{-j2\pi A_0 f}$ in both expressions (5) and (8). The frequencies at which the ground truth spectrum and the synthesized spectrum are compared are chosen to be $af_b + bf_h + i_0 f_r$, where $a = -5 : 5, b = -5 : 5$ and $i_0 = 20,000$. In other words, we are interested in up to the 5th order RR harmonic, the 5th order HR harmonic, and their intermods in the cluster centered at 5 GHz; this is basically a narrow band of frequencies centered at 5 GHz. The true spectrum is computed using (8) with $N = \lceil f_r T_w/2 \rceil = 4 \times 10^6$, and its approximation is computed using the synthesis formula (9) with $K = L = 20$, i.e., with only $41 \times 41$ terms. The error, $|H_w(f) - \widehat{H_w}(f)|$ does
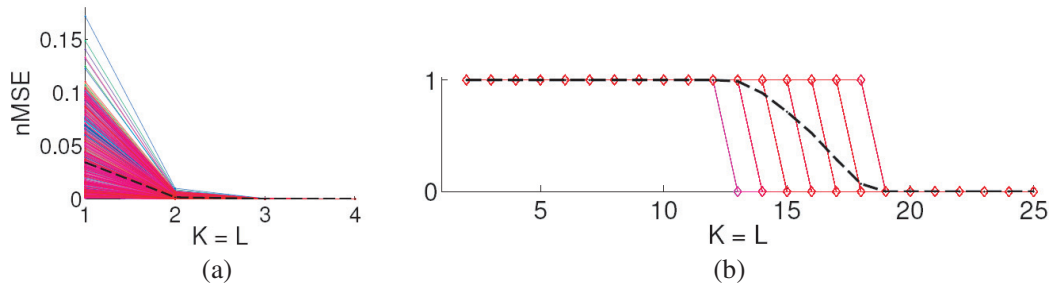
**Figure 8.** Numerical error analysis. (a) Normalized MSE (mean squared error normalized to the variance of the true spectrum) over random trials for the $m_h = m_b/14$ case. The plot is an overlay of 1000 curves and their average, which is represented by the dashed line. (b) Indication of whether the spectrum synthesized with a value of $K$ is different from that synthesized with $K-1$ for the $m_h = m_b/14$ case. The plot is an overlay of 1000 curves and their mean, which is represented by the dashed line.

not exceed 1.04, while the maximum value of $|H_w(f)|$ is about $1.2 \times 10^5$. The errors normalized to the standard deviation of the true spectrum are smaller than $0.71 \times 10^{-4}$ in magnitude. The mean squared error normalized to the variance of the true spectrum (nMSE) is $2.5 \times 10^{-9}$. Thus, our synthesized spectrum, using only a small number of terms, is extremely accurate.

We next present nMSE of the spectrum synthesis as a function of number of terms kept in a truncated version in Eq. (9). As in the example above, $T_w$ and $f_r$ are selected as in Table 2, and $A_0 = 0$. We generate 1000 random realizations of $[f_b, f_h, m_b]$, where $f_b \sim \mathcal{U}(0.2, 0.7)$ [Hz], $f_h \sim \mathcal{U}(0.8, 3.0)$ [Hz], and $m_b \sim \mathcal{U}(2, 8)$ [mm], for each of four cases: $m_h = m_b/14$, $m_h = m_b/32$, $m_h = m_b/64$, $m_h = m_b/128$ (thus, a total of four independent 1000-trial sets). For each trial, the true spectrum and synthesized spectrum are computed at the frequencies $af_b + bf_h + i_0 f_r$, where $a = -5 : 5$, $b = -5 : 5$, and $i_0 = 20,000$, as in the example above. For simplification, we set $L = K$. The nMSE versus $K = L$ for the random trials of the $m_h = m_b/14$ case is plotted in Fig. 8(a). The dashed line is obtained by averaging the nMSE curves. At $K = L = 1$ the worst case and average nMSEs are 17% and 4%, respectively. The nMSE quickly decreases as $K$ and $L$ increase and reduces to approximately $10^{-9}$ for $K = L \geq 3$. The nMSE graphs for the other three $m_b/m_h$ ratios are very similar qualitatively, hence are not shown.

Figure 8(b) indicates whether the spectrum synthesized with some value of $K$ is, under the equality test of MATLAB ("isequal" function), different from that synthesized with $K - 1$, for each random trial of the $m_h = m_b/16$ case. A "1" indicates difference and a zero value indicates equality. The dashed curve is the mean of the indicator functions. The graphs for the other three $m_b/m_h$ ratios are very similar, and it is observed that the synthesized results stop changing for $K \geq 19$ in all of the 4000 random trials. Since increasing $K$ and $L$ does not change the synthesized spectrum and therefore the error, we think that the error is caused by numerical computation.

Considering a pulse shape such as that in Fig. 2, the synthesis formula is easily obtained by replacing $c(f^*)$ in (9) by $c(f^*)P(f^*)$. The formula is then evaluated at more finely spaced frequencies and the resulting spectrum is plotted in Fig. 1. Here the synthesis excludes the $(k = 0, l = 0, i = i_0)$ component in the synthesis formula, which would be the "DC" component after frequency down conversion [37]. The graphs of the true spectrum and synthesized spectrum cannot be visually distinguished, and hence the former is not shown.

We have demonstrated that an accurate spectrum can be achieved by synthesizing with only a relatively small number of terms. These numerical results also validate the correctness of our mathematical derivation in this paper. The MATLAB code used in this paper will be published on http://www2.ece.gatech.edu/research/labs/sarl/.

## 5. COMPUTATIONAL COMPLEXITY COMPARISON

This section compares the computational complexity in terms of the number of multiplications of the CTFT formula and that of our model. Here we use $N_b'$ and $N_b''$ to distinguish the number of sines and the number of cosines in the breathing-induced delay model. Similarly, $N_h'$ and $N_h''$ are the

number of sines and the number of cosines in the heart-beating-induced delay model. Thus, in Eq. (1), $N_b = \max(N_b', N_b'')$ and $N_h = \max(N_h', N_h'')$.

The number of multiplications in the CTFT formula is $(f_r T_w + 1)(5N_b' + 5N_b'' + 5N_h' + 5N_h'' + 4)$. The number of multiplications in our model of $H_w(f)$ is $(i_{\max} - i_{\min} + 1)(2N_b' + 2N_b'' + 2N_h' + 2N_h'' + 11)(2K + 1)^{(N_b' + N_b'')}(2L + 1)^{(N_h' + N_h'')}$.

The complexity of the CTFT formula linearly increases with $f_r, T_w, N_b, N_b', N_h, N_h'$. The complexity of our model exponentially increases with $N_b, N_b', N_h, N_h'$ but does not depend on $f_r$ and $T_w$. $[i_{\min}, i_{\max}]$ is the range of cluster indices $i$ that contribute to the spectrum at a frequency of interest. However, for practical value of $f_r$ (on the order of kHz or MHz) and $T_w$ (on the order of seconds), $i_{\min} = i_{\max} = i^*$ where $i^*$ is the cluster of the frequency range of interest.

*Example 1*: $f_r$ and $T_w$ are as in Table 2, $K = L = 20, i_{\max} = i_{\min}$. For the delay model used is Eq. (3), $N_b' = N_h' = 1, N_b'' = N_h'' = 0$. The number of multiplications in the CTFT formula and our model are $1.12 \times 10^8$ and $2.5 \times 10^4$, respectively. In this case, the complexity of our model is three order of magnitudes less than that of the CTFT formula.

*Example 2*: However, when there are five sinusoids in the model, the complexity of our model is 10 times higher than the CTFT formula.

The ratio between the complexity of our model and that of the CTFT is plotted in Fig. 9 for various values of the pulse repetition frequency $f_r$. These $f_r$ values are manually collected from experimental settings of IR-UWB radar systems of many different groups [1, 10, 16, 38–40]. The horizontal bold dashed line indicates where our model has the same complexity with that of the CTFT. A value below this line indicates that our model has less complexity than the CTFT formula, and a value above this line indicates otherwise. Our model is able to achieve computational complexity reduction of several orders of magnitudes compared to the CTFT formula when the displacement model has a small number of sinusoids, but becomes more computationally expensive with more complex displacement functions. Additionally, the ratio curves when plotted in logarithmic scale almost linearly increase with the number of sinusoids in the displacement model. For a given number of sinusoids, the ratio decreases as $f_r$ increases, since the complexity of the CTFT formula increases with $f_r$ whereas our complexity does not depend on $f_r$. As a numerical check for this, computation time of the two formulas is measured with MATLAB 2015b on an Intel(R) Core(TM) i7-4870HQ CPU @ 2.50GHz laptop computer. Table 3 shows the computation time for the displacement model in Eq. (3) for various values of $f_r$.

We conclude that for a small number of sines and cosines in the delay model, our spectrum model has less computational complexity. Exact complexity difference depend on system variables including $f_r$, $T_w$, the number of sinusoids in the displacement model, and the number of terms retained in the synthesis formula $(K, L)$.
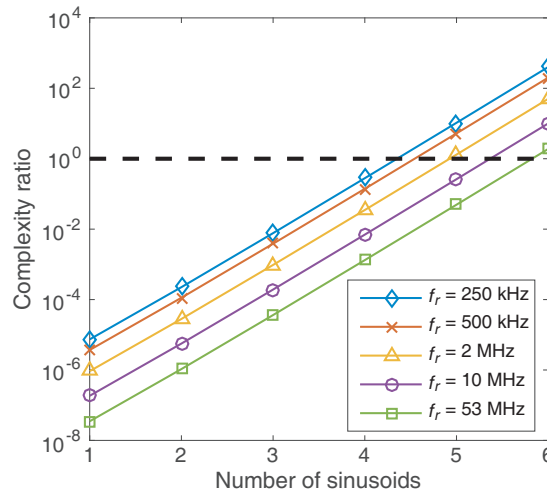


**Figure 9.** The ratio between the complexity of our model and that of the CTFT.

**Table 3.** Computation time of the CTFT formula and that of our model for a two-sinusoid displacement model.

| $f_r$ | Our model | CTFT formula |
|---|---|---|
| $250\,\mathrm{kHz}$ | $0.0249\,\mathrm{s}$ | $141.3\,\mathrm{s}$ |
| $500\,\mathrm{kHz}$ | $0.0233\,\mathrm{s}$ | $277.1\,\mathrm{s}$ |
| $2\,\mathrm{MHz}$ | $0.0239\,\mathrm{s}$ | $1,102.8\,\mathrm{s}$ |
| $10\,\mathrm{MHz}$ | $0.0238\,\mathrm{s}$ | $5,351.0\,\mathrm{s}$ |
| $53\,\mathrm{MHz}$ | $0.0242\,\mathrm{s}$ | $27,510.0\,\mathrm{s}$ |

## 6. CONCLUSION

In this paper, we have developed the first generic modeling framework for the reflected IR-UWB signal as it arrives at the radar receive antenna, for chest displacement due to arbitrary periodic heart and lungs motion. No assumption on the phase of these periodic movements has been made. Closed-form expressions of both the complex amplitude and frequency of each spectral component are provided. Our analysis shows that the radar received signal spectrum has components located at multiples of RR, multiples of HR, multiples of the burst repetition frequency, and their intermodulation products. Although the analysis is done assuming only a planar air-skin interface, extension to a multi-layered planar thorax model is straightforward through superposition.

For the sum-of-two-sinusoids chest displacement model, our analysis shows that the radar received signal spectrum comprises sparsely-located clusters, each of which has only a few significant components. The relative amplitudes of the components within a cluster are shown to vary significantly from cluster to cluster over the UWB band of 3 to $10\,\mathrm{GHz}$ and are a function of maximum chest displacement. Also, the previously reported aliased spectrum is shown to differ significantly from the un-aliased spectrum presented in this paper. Practicality and usage of our analytical model is discussed in terms of the number of significant terms and numerical precision.

The presented model has several advantages over just using the CTFT. The CTFT expression does not reveal the locations of spectral components nor, because of the nonlinear nature of delay modulation, does it clarify how a particular sinusoidal component of the displacement function contributes to the spectrum. The cluster structure of our model allows convenient inspection of cluster-to-cluster variations. This provides a foundation for the detection of particular patterns of breathing by comparing clusters. However, a limitation of our model is that the total number of multiplications in our model will exceed that of the CTFT for more complex displacement functions.

## ACKNOWLEDGMENT

## APPENDIX A. RADAR RECEIVED SPECTRUM FOR A PERIODIC CHEST DISPLACEMENT MODEL

In this derivation, we utilize Fourier theory and Jacobi-Anger expansions. To reduce complexity, assume the DC component in Eq. (1) is zero, i.e., $A_0 = 0$. When $A_0 \neq 0$, the resulting expression will be simply multiplied by $e^{-j2\pi A_0 f}$. We will use the following notations: $\Omega = 2\pi f, \Omega_b = 2\pi f_b, \Omega_h = 2\pi f_h$. We begin with $H(f) = \sum\limits_{n=-\infty}^{\infty} e^{-j\Omega n T_r} e^{-j\Omega \tau_{d,n}}$. Into $e^{-j\Omega \tau_{d,n}}$, we substitute $\tau_{d,n} = \tau_d(nT_r)$ using (1), and apply the property $\exp\{\sum_k \alpha_k\} = \prod\limits_k \exp\{\alpha_k\}$ to get a product with four factors of similar form; two of them are $\prod\limits_{p=1}^{N_b} \exp\{-j\Omega B_p^b \sin p\Omega_b n T_r\}$ and $\prod\limits_{q'=1}^{N_h} \exp\{-j\Omega A_{q'}^h \cos q'\Omega_h n T_r\}$. Based on the Jacobi–Anger expansion $e^{jz\sin\theta} = \sum\limits_{n=-\infty}^{\infty} J_n(z)e^{jn\theta}$ and $e^{jz\cos\theta} = \sum\limits_{n=-\infty}^{\infty} j^n J_n(z)e^{jn\theta}$, where $J_n(z)$ is the

Bessel function of the first kind of order $n$, it is trivial to prove that $e^{-jz\sin\theta} = \sum\limits_{n=-\infty}^{\infty} J_n(z)e^{-jn\theta}$ and

$e^{-jz\cos\theta} = \sum\limits_{n=-\infty}^{\infty} j^{-n}J_n(z)e^{-jn\theta}$. Applying these, we may express $e^{-j\Omega\tau_{d,n}}$ as

$$\prod_{p=1}^{N_b}\sum_{k_p=-\infty}^{\infty} J_{k_p}(\Omega B_p^b)e^{-jk_p p\Omega_b nT_r} \times \prod_{p'=1}^{N_b}\sum_{k'_{p'}=-\infty}^{\infty} J_{k'_{p'}}(\Omega A_{p'}^b)j^{-k'_{p'}}e^{-jk'_{p'}p'\Omega_b nT_r}$$

$$\times \prod_{q=1}^{N_h}\sum_{l_q=-\infty}^{\infty} J_{l_q}(\Omega B_q^h)e^{-jl_q q\Omega_h nT_r} \times \prod_{q'=1}^{N_h}\sum_{l'_{q'}=-\infty}^{\infty} J_{l'_{q'}}(\Omega A_{q'}^h)j^{-l'_{q'}}e^{-jl'_{q'}q'\Omega_h nT_r}.$$

After applying the distributive law across all summations (there are $2N_b + 2N_h + 1$ of them in general) and defining the following notations

$$\sum_{\mathbb{K}} = \sum_{k_1}\sum_{k_2}\cdots\sum_{k_{N_b}}\sum_{k'_1}\sum_{k'_2}\cdots\sum_{k'_{N_b}}\sum_{l_1}\sum_{l_2}\cdots\sum_{l_{N_h}}\sum_{l'_1}\sum_{l'_2}\cdots\sum_{l'_{N_h}},$$

where $\mathbb{K} = [k_1, \ldots, k_{N_b}, k'_1, \ldots, k'_{N_b}, l_1, \ldots, l_{N_h}, l'_1, \ldots, l'_{N_h}]$,

$$\begin{aligned}\mathbb{J}(\alpha, \mathbb{K}, \Omega) &= J_{\alpha k_1}(\Omega B_1^b)J_{\alpha k_2}(\Omega B_2^b)\cdots J_{\alpha k_{N_b}}(\Omega B_{N_b}^b)\\ &\cdot J_{\alpha k'_1}(\Omega A_1^b)J_{\alpha k'_2}(\Omega A_2^b)\cdots J_{\alpha k'_{N_b}}(\Omega A_{N_b}^b)\\ &\cdot J_{\alpha l_1}(\Omega B_1^h)J_{\alpha l_2}(\Omega B_2^h)\cdots J_{\alpha l_{N_h}}(\Omega B_{N_h}^h)\\ &\cdot J_{\alpha l'_1}(\Omega A_1^h)J_{\alpha l'_2}(\Omega A_2^h)\cdots J_{\alpha l'_{N_h}}(\Omega A_{N_h}^h)\\ &\cdot j^{-\alpha(k'_1+k'_2+\ldots+k'_{N_b}+l'_1+l'_2+\ldots+l'_{N_h})},\end{aligned} \tag{A1}$$

$$\begin{aligned}\bullet &= \left((k_1 + k'_1) + 2(k_2 + k'_2) + \ldots + N_b(k_{N_b} + k'_{N_b})\right)f_b\\ &+ \left((l_1 + l'_1) + 2(l_2 + l'_2) + \ldots + N_h(l_{N_h} + l'_{N_h})\right)f_h\\ &= \left[\sum_{p=1}^{N_b} p(k_p + k'_p)\right]f_b + \left[\sum_{q=1}^{N_h} q(l_q + l'_q)\right]f_h,\end{aligned}$$

where $\alpha \in \{-1, 1\}$, it is tedious but straightforward to show that

$$H(f) = \sum_{\mathbb{K}} \mathbb{J}(1, \mathbb{K}, 2\pi f)\sum_n e^{-j2\pi(f+\bullet)nT_r}. \tag{A2}$$

Applying $\sum\limits_{n=-\infty}^{\infty} e^{-j2\pi fnT} = \frac{1}{T}\sum\limits_{m=-\infty}^{\infty} \delta\left(f - \frac{m}{T}\right)$ to the last summation in Eq. (A2), and using $f_r = 1/T_r$, we obtain:

$$\begin{aligned}H(f) &= \sum_{\mathbb{K}} \mathbb{J}(1, \mathbb{K}, 2\pi f)f_r\sum_{i=-\infty}^{\infty} \delta(f + \bullet - if_r)\\ &= f_r\sum_{\mathbb{K}}\sum_i \mathbb{J}(1, \mathbb{K}, 2\pi f)\delta(f + \bullet - if_r)\\ &= f_r\sum_{\mathbb{K}}\sum_i \mathbb{J}(-1, \mathbb{K}, 2\pi f)\delta(f - \bullet - if_r).\end{aligned} \tag{A3}$$

Since $J_{-n}(x) = (-1)^n J_n(x)$ for $n \in Z$, Eq. (A3) becomes

$$H(f) = \sum_{\mathbb{K}}\sum_i f_r(-1)^{k_1+k_2+\ldots+k_{N_b}+l_1+l_2+\ldots+l_{N_h}}\mathbb{J}(1, \mathbb{K}, 2\pi f)\delta(f - \bullet - if_r)$$

By moving the summation $\sum_i$ to the front, replacing $\mathbb{J}(1, \mathbb{K}, 2\pi f)$ with its definition in Eq. (A1), and including $e^{-j2\pi A_0 f}$, we obtain Eq. (2).

## REFERENCES

1. Li, W. Z., Z. Li, H. Lv, G. Lu, Y. Zhang, X. Jing, S. Li, and J. Wang, "A new method for non-line-of-sight vital sign monitoring based on developed adaptive line enhancer using low centre frequency UWB radar," *Progress In Electromagnetics Research*, Vol. 133, 535–554, 2013.

2. Li, Y., X. Jing, H. Lv, and J. Wang, "Analysis of characteristics of two close stationary human targets detected by impulse radio UWB radar," *Progress In Electromagnetics Research*, Vol. 126, 429–447, 2012.

3. Li, J., et al., "Through-wall detection of human being's movement by UWB radar," *IEEE Geoscience and Remote Sensing Letters*, Vol. 9, No. 6, 1079–1083, 2012.

4. Lazaro, A., D. Girbau, and R. Villarino, "Wavelet-based breast tumor localization technique using a UWB radar," *Progress In Electromagnetics Research*, Vol. 98, 75–95, 2009.

5. Zhang, H., S. Y. Tan, and H. S. Tan, "A novel method for microwave breast cancer detection," *Progress In Electromagnetics Research*, Vol. 83, 413–434, 2008.

6. Conceicao, R. C., M. O'Halloran, M. Glavin, and E. Jones, "Support vector machines for the classification of early-stage breast cancer based on radar target signatures," *Progress In Electromagnetics Research B*, Vol. 23, 311–327, 2010.

7. AlShehri, S. A. and S. Khatun, "UWB imaging for breast cancer detection using neural network," *Progress In Electromagnetics Research C*, Vol. 7, 79–93, 2009.

8. Nguyen, V., A. Javaid, and M. A. Weitnauer, "Detection of motion and posture change using an IR-UWB radar," *IEEE Int. Conf. Eng. Medicine and Biology Society (EMBC)*, 2016.

9. AlShehri, S. A., S. Khatun, A. B. Jantan, R. S. A. Raja Abdullah, R. Mahmud, and Z. Awang, "3d experimental detection and discrimination of malignant and benign breast tumor using nn-based UWB imaging system," *Progress In Electromagnetics Research*, Vol. 116, 221–237, 2011.

10. Xu, Y., S. Dai, S. Wu, J. Chen, and G. Fang, "Vital sign detection method based on multiple higher order cumulant for ultrawideband radar," *IEEE Transactions on Geoscience and Remote Sensing*, Vol. 50, No. 4, 1254–1265, 2012.

11. Lai, J. C., et al., "Wireless sensing of human respiratory parameters by low-power ultrawideband impulse radio radar," *IEEE Trans. on Instrumentation and Measurement*, Vol. 60, No. 3, 928–938, 2011.

12. Nguyen, V., A. Q. Javaid, and M. A. Weitnauer, "Harmonic Path (HAPA) algorithm for noncontact vital signs monitoring with IR-UWB radar," *IEEE Biomedical Circuits and Systems Conference (BioCAS)*, 146–149, 2013.

13. Nguyen, V., A. Javaid, and M. A. Weitnauer, "Spectrum-averaged Harmonic Path (SHAPA) algorithm for non-contact vital sign monitoring with Ultra-Wideband (UWB) radar," *IEEE International Conference of the IEEE Engineering in Medicine and Biology Society (EMBC)*, 2241–2244, 2014.

14. Venkatesh, S., et al., "Implementation and analysis of respiration-rate estimation using impulsebased UWB," *IEEE Mil. Comm. Conf.*, 3314–3320, 2005.

15. Mabrouk, M., et al., "Model of human breathing re ected signal received by PN-UWB radar," *IEEE International Conference of the IEEE Engineering in Medicine and Biology Society (EMBC)*, 4559–4562, 2014.

16. Lazaro, A., D. Girbau, and R. Villarino, "Analysis of vital signs monitoring using an IR-UWB radar," *Progress In Electromagnetics Research*, Vol. 100, 265–284, 2010.

17. Donelli, M., "A rescue radar system for the detection of victims trapped under rubble based on the independent component analysis algorithm," *Progress In Electromagnetics Research M*, Vol. 19, 173–181, 2011.

18. Li, C., J. Ling, J. Li, and J. Lin, "Accurate doppler radar noncontact vital sign detection using the relax algorithm," *IEEE Transactions on Instrumentation and Measurement*, Vol. 59, No. 3, 687–695, 2010.

19. Zakrzewski, M., A. Vehkaoja, A. S. Joutsen, K. T. Palovuori, and J. J. Vanhala, "Noncontact respiration monitoring during sleep with microwave doppler radar," *IEEE Sensors Journal*, Vol. 15,

No. 10, 5683–5693, 2015.

20. Pozar, D. M., "Waveform optimizations for ultrawideband radio systems," *IEEE Transactions on Antennas and Propagation*, Vol. 51, No. 9, 2335–2345, 2003.

21. Staderini, E. M., "UWB radars in medicine," *IEEE Aerospace and Electronic Systems Magazine*, Vol. 17, No. 1, 13–18, 2002.

22. Bucci, O. M., T. Isernia, and A. F. Morabito, "Optimal synthesis of circularly symmetric shaped beams," *IEEE Transactions on Antennas and Propagation*, Vol. 62, No. 4, 1954–1964, 2014.

23. Poletti, M. A., "Three-dimensional surround sound systems based on spherical harmonics," *Journal of the Audio Engineering Society*, Vol. 53, No. 11, 1004–1025, 2005.

24. Kay, S. M., *Fundamentals of Statistical Signal Processing: Practical Algorithm Development*, Vol. 3. Pearson Education, 2013.

25. Arulampalam, M. S., S. Maskell, N. Gordon, and T. Clapp, "A tutorial on particle filters for onne nonlinear/non-gaussian bayesian tracking," *IEEE Transactions on Signal Processing*, Vol. 50, No. 2, 174–188, 2002.

26. Lai, Y. and Y. Fu, "Method and system for reliable inspiration-to-expiration ratio extraction from acoustic physiological signal," US Patent App. 12/800,932, Dec. 1, 2011.

27. Pandia, K., O. T. Inan, G. T. Kovacs, and L. Giovangrandi, "Extracting respiratory information from seismocardiogram signals acquired on the chest using a miniature accelerometer," *Physiological Measurement*, Vol. 33, No. 10, 1643, 2012.

28. Thompson, W. B., M. B. Rappaport, and H. B. Sprague, "Ballistocardiography ii. The normal ballistocardiogram," *Circulation*, Vol. 7, No. 3, 321–328, 1953.

29. Oppenheim, A. V. and R. W. Schafer, *Discrete-time Signal Processing*, Pearson, 2010.

30. Foo, S., "Ultra wideband monitoring systems and antennas," US Patent 8,428,696, Apr. 23 2013.

31. Nguyen, V. and M. A. Weitnauer, "UWB impulse radar for vital signs sensing — A modeling framework for arbitrary periodic heart and lung motion," *IEEE Biomedical Circuits and Systems Conference (BioCAS)*, 2015.

32. Staderini, E. M. and G. Varotto, "Optimization criteria in the design of medical UWB radars in compliance with the regulatory masks," *IEEE Biomedical Circuits and Systems Conference (BioCAS)*, 53–58, 2007.

33. Fontana, R. J., "Recent system applications of short-pulse ultra-wideband (UWB) technology," *IEEE Transactions on Microwave Theory and Techniques*, Vol. 52, No. 9, 2087–2104, 2004.

34. Hu, B. and N. C. Beaulieu, "Pulse shapes for ultrawideband communication systems," *IEEE Transactions on Wireless Communications*, Vol. 4, No. 4, 1789–1797, 2005.

35. Schwartz, C., "Numerical calculation of bessel functions," *International Journal of Modern Physics C*, Vol. 23, No. 12, 1250084, 2012.

36. Du Toit, C. F., "The numerical computation of bessel functions of the first and second kind for integer orders and complex arguments," *IEEE Transactions on Antennas and Propagation*, Vol. 38, No. 9, 1341–1349, 1990.

37. Barry, J. R., E. A. Lee, and D. G. Messerschmitt, *Digital Communication*, Springer Science & Business Media, 2004.

38. Immoreev, I. Y., "Practical applications of uwb technology," *IEEE Aerospace and Electronic Systems Magazine*, Vol. 25, No. 2, 36–42, 2010.

39. Hsieh, C.-H., Y.-F. Chiu, Y.-H. Shen, T.-S. Chu, and Y.-H. Huang, "A uwb radar signal processing platform for real-time human respiratory feature extraction based on four-segment linear waveform model," *IEEE Transactions on Biomedical Circuits and Systems*, Vol. 10, No. 1, 219–230, 2016.

40. Pittella, E., S. Pisa, and M. Cavagnaro, "Breath activity monitoring with wearable UWB radars: Measurement and analysis of the pulses re ected by the human body," *IEEE Transactions on Bio-medical Engineering*, 2015.